Observation of an alternative χ_{c0}(2P) candidate in e^{+}e^{-}→J/ψDD[over ¯]

K. Chilikin *et al.* (Belle Collaboration)

Phys. Rev. D **95**, 112003 — Published 16 June 2017

DOI: 10.1103/PhysRevD.95.112003

Observation of an alternative $\chi_{c0}(2P)$ candidate in $e^+e^- \to J/\psi D\bar{D}$

K. Chilikin,[39,47] I. Adachi,[13,10] H. Aihara,[74] S. Al Said,[68,33] D. M. Asner,[58] V. Aulchenko,[3,56] R. Ayad,[68] V. Babu,[69] I. Badhrees,[68,32] A. M. Bakich,[67] V. Bansal,[58] E. Barberio,[45] D. Besson,[47] V. Bhardwaj,[16] B. Bhuyan,[18] J. Biswal,[27] A. Bobrov,[3,56] A. Bondar,[3,56] A. Bozek,[53] M. Bračko,[43,27] T. E. Browder,[12] D. Červenkov,[4] V. Chekelian,[44] A. Chen,[50] B. G. Cheon,[11] K. Cho,[34] Y. Choi,[66] D. Cinabro,[79] N. Dash,[17] S. Di Carlo,[79] Z. Doležal,[4] Z. Drásal,[4] D. Dutta,[69] S. Eidelman,[3,56] H. Farhat,[79] J. E. Fast,[58] T. Ferber,[7] B. G. Fulsom,[58] V. Gaur,[78] N. Gabyshev,[3,56] A. Garmash,[3,56] R. Gillard,[79] P. Goldenzweig,[30] J. Haba,[13,10] T. Hara,[13,10] K. Hayasaka,[55] W.-S. Hou,[52] K. Inami,[49] A. Ishikawa,[72] R. Itoh,[13,10] Y. Iwasaki,[13] W. W. Jacobs,[20] I. Jaegle,[8] H. B. Jeon,[37] Y. Jin,[74] D. Joffe,[31] K. K. Joo,[5] T. Julius,[45] K. H. Kang,[37] G. Karyan,[7] P. Katrenko,[48,39] D. Y. Kim,[64] H. J. Kim,[37] J. B. Kim,[35] K. T. Kim,[35] M. J. Kim,[37] S. H. Kim,[11] Y. J. Kim,[34] K. Kinoshita,[6] P. Kodyš,[4] S. Korpar,[43,27] D. Kotchetkov,[12] P. Križan,[40,27] P. Krokovny,[3,56] T. Kuhr,[41] R. Kulasiri,[31] A. Kuzmin,[3,56] Y.-J. Kwon,[81] J. S. Lange,[9] L. Li,[61] L. Li Gioi,[44] J. Libby,[19] D. Liventsev,[78,13] M. Lubej,[27] T. Luo,[59] M. Masuda,[73] T. Matsuda,[46] D. Matvienko,[3,56] K. Miyabayashi,[82] H. Miyata,[55] R. Mizuk,[39,47,48] G. B. Mohanty,[69] H. K. Moon,[35] T. Mori,[49] R. Mussa,[25] E. Nakano,[57] M. Nakao,[13,10] T. Nanut,[27] K. J. Nath,[18] Z. Natkaniec,[53] M. Nayak,[79,13] M. Niiyama,[36] N. K. Nisar,[59] S. Nishida,[13,10] S. Ogawa,[71] S. Okuno,[28] S. L. Olsen,[29] H. Ono,[54,55] P. Pakhlov,[39,47] G. Pakhlova,[39,48] B. Pal,[6] S. Pardi,[24] H. Park,[37] S. Paul,[70] R. Pestotnik,[27] L. E. Piilonen,[78] C. Pulvermacher,[13] M. Ritter,[41] H. Sahoo,[12] Y. Sakai,[13,10] M. Salehi,[42,41] S. Sandilya,[6] L. Santelj,[13] T. Sanuki,[72] O. Schneider,[38] G. Schnell,[1,15] C. Schwanda,[22] Y. Seino,[55] K. Senyo,[80] O. Seon,[49] M. E. Sevior,[45] V. Shebalin,[3,56] C. P. Shen,[2] T.-A. Shibata,[75] J.-G. Shiu,[52] A. Sokolov,[23] E. Solovieva,[39,48] M. Starič,[27] T. Sumiyoshi,[76] M. Takizawa,[63,14,60] U. Tamponi,[25,77] K. Tanida,[26] F. Tenchini,[45] K. Trabelsi,[13,10] M. Uchida,[75] S. Uehara,[13,10] T. Uglov,[39,48] S. Uno,[13,10] Y. Usov,[3,56] C. Van Hulse,[1] G. Varner,[12] A. Vinokurova,[3,56] A. Vossen,[20] C. H. Wang,[51] M.-Z. Wang,[52] P. Wang,[21] M. Watanabe,[55] Y. Watanabe,[28] E. Widmann,[65] E. Won,[35] H. Yamamoto,[72] Y. Yamashita,[54] H. Ye,[7] C. Z. Yuan,[21] Y. Yusa,[55] Z. P. Zhang,[61] V. Zhilich,[3,56] V. Zhulanov,[3,56] and A. Zupanc[40,27]

(The Belle Collaboration)

[1] *University of the Basque Country UPV/EHU, 48080 Bilbao*
[2] *Beihang University, Beijing 100191*
[3] *Budker Institute of Nuclear Physics SB RAS, Novosibirsk 630090*
[4] *Faculty of Mathematics and Physics, Charles University, 121 16 Prague*
[5] *Chonnam National University, Kwangju 660-701*
[6] *University of Cincinnati, Cincinnati, Ohio 45221*
[7] *Deutsches Elektronen–Synchrotron, 22607 Hamburg*
[8] *University of Florida, Gainesville, Florida 32611*
[9] *Justus-Liebig-Universität Gießen, 35392 Gießen*
[10] *SOKENDAI (The Graduate University for Advanced Studies), Hayama 240-0193*
[11] *Hanyang University, Seoul 133-791*
[12] *University of Hawaii, Honolulu, Hawaii 96822*
[13] *High Energy Accelerator Research Organization (KEK), Tsukuba 305-0801*
[14] *J-PARC Branch, KEK Theory Center, High Energy Accelerator Research Organization (KEK), Tsukuba 305-0801*
[15] *IKERBASQUE, Basque Foundation for Science, 48013 Bilbao*
[16] *Indian Institute of Science Education and Research Mohali, SAS Nagar, 140306*
[17] *Indian Institute of Technology Bhubaneswar, Satya Nagar 751007*
[18] *Indian Institute of Technology Guwahati, Assam 781039*
[19] *Indian Institute of Technology Madras, Chennai 600036*
[20] *Indiana University, Bloomington, Indiana 47408*
[21] *Institute of High Energy Physics, Chinese Academy of Sciences, Beijing 100049*
[22] *Institute of High Energy Physics, Vienna 1050*
[23] *Institute for High Energy Physics, Protvino 142281*
[24] *INFN - Sezione di Napoli, 80126 Napoli*
[25] *INFN - Sezione di Torino, 10125 Torino*
[26] *Advanced Science Research Center, Japan Atomic Energy Agency, Naka 319-1195*
[27] *J. Stefan Institute, 1000 Ljubljana*
[28] *Kanagawa University, Yokohama 221-8686*
[29] *Center for Underground Physics, Institute for Basic Science, Daejeon 34047*
[30] *Institut für Experimentelle Kernphysik, Karlsruher Institut für Technologie, 76131 Karlsruhe*
[31] *Kennesaw State University, Kennesaw, Georgia 30144*
[32] *King Abdulaziz City for Science and Technology, Riyadh 11442*
[33] *Department of Physics, Faculty of Science, King Abdulaziz University, Jeddah 21589*
[34] *Korea Institute of Science and Technology Information, Daejeon 305-806*

[35]*Korea University, Seoul 136-713*
[36]*Kyoto University, Kyoto 606-8502*
[37]*Kyungpook National University, Daegu 702-701*
[38]*École Polytechnique Fédérale de Lausanne (EPFL), Lausanne 1015*
[39]*P.N. Lebedev Physical Institute of the Russian Academy of Sciences, Moscow 119991*
[40]*Faculty of Mathematics and Physics, University of Ljubljana, 1000 Ljubljana*
[41]*Ludwig Maximilians University, 80539 Munich*
[42]*University of Malaya, 50603 Kuala Lumpur*
[43]*University of Maribor, 2000 Maribor*
[44]*Max-Planck-Institut für Physik, 80805 München*
[45]*School of Physics, University of Melbourne, Victoria 3010*
[46]*University of Miyazaki, Miyazaki 889-2192*
[47]*Moscow Physical Engineering Institute, Moscow 115409*
[48]*Moscow Institute of Physics and Technology, Moscow Region 141700*
[49]*Graduate School of Science, Nagoya University, Nagoya 464-8602*
[50]*National Central University, Chung-li 32054*
[51]*National United University, Miao Li 36003*
[52]*Department of Physics, National Taiwan University, Taipei 10617*
[53]*H. Niewodniczanski Institute of Nuclear Physics, Krakow 31-342*
[54]*Nippon Dental University, Niigata 951-8580*
[55]*Niigata University, Niigata 950-2181*
[56]*Novosibirsk State University, Novosibirsk 630090*
[57]*Osaka City University, Osaka 558-8585*
[58]*Pacific Northwest National Laboratory, Richland, Washington 99352*
[59]*University of Pittsburgh, Pittsburgh, Pennsylvania 15260*
[60]*Theoretical Research Division, Nishina Center, RIKEN, Saitama 351-0198*
[61]*University of Science and Technology of China, Hefei 230026*
[62]*Seoul National University, Seoul 151-742*
[63]*Showa Pharmaceutical University, Tokyo 194-8543*
[64]*Soongsil University, Seoul 156-743*
[65]*Stefan Meyer Institute for Subatomic Physics, Vienna 1090*
[66]*Sungkyunkwan University, Suwon 440-746*
[67]*School of Physics, University of Sydney, New South Wales 2006*
[68]*Department of Physics, Faculty of Science, University of Tabuk, Tabuk 71451*
[69]*Tata Institute of Fundamental Research, Mumbai 400005*
[70]*Department of Physics, Technische Universität München, 85748 Garching*
[71]*Toho University, Funabashi 274-8510*
[72]*Department of Physics, Tohoku University, Sendai 980-8578*
[73]*Earthquake Research Institute, University of Tokyo, Tokyo 113-0032*
[74]*Department of Physics, University of Tokyo, Tokyo 113-0033*
[75]*Tokyo Institute of Technology, Tokyo 152-8550*
[76]*Tokyo Metropolitan University, Tokyo 192-0397*
[77]*University of Torino, 10124 Torino*
[78]*Virginia Polytechnic Institute and State University, Blacksburg, Virginia 24061*
[79]*Wayne State University, Detroit, Michigan 48202*
[80]*Yamagata University, Yamagata 990-8560*
[81]*Yonsei University, Seoul 120-749*
[82]*Nara Women's University, Nara 630-8506*

We perform a full amplitude analysis of the process $e^+e^- \to J/\psi D\bar{D}$, where D refers to either D^0 or D^+. A new charmoniumlike state $X^*(3860)$ that decays to $D\bar{D}$ is observed with a significance of 6.5σ. Its mass is $(3862^{+26}_{-32}{}^{+40}_{-13})$ MeV/c^2 and width is $(201^{+154}_{-67}{}^{+88}_{-82})$ MeV. The $J^{PC} = 0^{++}$ hypothesis is favored over the 2^{++} hypothesis at the level of 2.5σ. The analysis is based on the 980 fb^{-1} data sample collected by the Belle detector at the asymmetric-energy e^+e^- collider KEKB.

PACS numbers: 14.40.Pq,13.25.Gv,13.66.Bc

I. INTRODUCTION

The charmoniumlike state $X(3915)$ was observed by the Belle Collaboration in $B \to J/\psi\omega K$ decays [1]; its original name was the $Y(3940)$. Subsequently, it was also observed by the *BABAR* Collaboration in the same B decay mode [2, 3] and by both Belle [4] and *BABAR* [5] in the process $\gamma\gamma \to X(3915) \to J/\psi\omega$. The quantum numbers of the $X(3915)$ were measured in Ref. [5] to be $J^{PC} = 0^{++}$. As a result, the $X(3915)$ was identified as the $\chi_{c0}(2P)$ in the 2014 PDG tables [6].

However, this identification remains in doubt. The $\chi_{c0}(2P)$ is expected to decay strongly to $D\bar{D}$ in an S-wave. Here and elsewhere, D refers to either D^0 or D^+. The $\chi_{c0}(2P) \to D\bar{D}$ decay mode is expected to be dominant, but has not yet been observed experimentally for the $X(3915)$; in contrast, the decay mode that is observed, $X(3915) \to J/\psi\omega$, would be OZI (Okubo-Zweig-Iizuka) [7] suppressed for the $\chi_{c0}(2P)$. Since the $\chi_{c0}(2P)$ should decay to $D\bar{D}$ in an S-wave, this state is naïvely expected to have a large width of $\Gamma \gtrsim 100$ MeV [8]; however, the measured $X(3915)$ width of (20 ± 5) MeV is much smaller. We note that there are some specific predictions for the $\chi_{c0}(2P)$ width that give small values. For example, the predicted width is 30 MeV in Ref. [9] and between 12 and ∼100 MeV, depending on the $\chi_{c0}(2P)$ mass, in Ref. [10]. If the $\chi_{c0}(2P)$ and $X(3915)$ are the same state, then the partial width to $J/\psi\omega$, which has been estimated to be $\Gamma(\chi_{c0}(2P) \to J/\psi\omega) \gtrsim 1$ MeV [8], is too large. Also, in this case, one can obtain contradictory estimates for the branching fraction $\mathcal{B}(\chi_{c0}(2P) \to J/\psi\omega)$ [11]. Furthermore, the $\chi_{c2}(2P) - \chi_{c0}(2P)$ mass splitting would be much smaller than the prediction of potential models and smaller than the mass difference for the bottomonium states $\chi_{bJ}(2P)$ [8, 11], which is inconsistent with expectations based on the heavier bottom quark mass.

The quantum numbers of the $X(3915)$ were measured in Ref. [5] to be $J^{PC} = 0^{++}$ assuming that the $X(3915)$ is produced in the process $\gamma\gamma \to X(3915)$ with helicity $\lambda = 2$ if its quantum numbers are $J^{PC} = 2^{++}$. A reanalysis of the data from Ref. [5], presented in Ref. [12], shows that the 2^{++} assignment becomes possible if the $\lambda = 2$ assumption is abandoned. As a result of these considerations, the $X(3915)$ is no longer identified as the $\chi_{c0}(2P)$ in the 2016 PDG tables [13].

It is possible that an alternative $\chi_{c0}(2P)$ candidate was actually observed by Belle [14] and *BABAR* [15] in the process $\gamma\gamma \to D\bar{D}$ together with the $\chi_{c2}(2P)$. An alternative fit to Belle and *BABAR* data was performed in Ref. [8]. In this fit, the nonresonant $\gamma\gamma \to D\bar{D}$ events are attributed to a wide charmonium state with mass and width $M = (3838 \pm 12)$ MeV/c^2 and $\Gamma = (211 \pm 19)$ MeV. However, in this estimate, additional signal sources such as feed-down from $\gamma\gamma \to D\bar{D}^*$ events were not taken into account; consequently, if the $\chi_{c0}(2P)$ is really observed in the process $\gamma\gamma \to D\bar{D}$, then the parameters measured in Ref. [8] are biased — the $\chi_{c0}(2P)$ mass is shifted to lower values [11].

It is also possible to search for the $\chi_{c0}(2P)$ produced in the process $\gamma\gamma \to \chi_{c0}(2P)$ using final states other than $D\bar{D}$ and $J/\psi\omega$. Belle searched for high-mass charmonium states in the process $\gamma\gamma \to K^0_S K^0_S$ [18]. An excess with a marginal statistical significance of 2.6σ was found in the mass region between 3.80 and 3.95 GeV/c^2.

A unique process that is suitable for a search for the $\chi_{c0}(2P)$ and other charmonium states with positive C-parity is double-charmonium production in association with the J/ψ. The C-parity of the states observed with the J/ψ is guaranteed to be positive in the case of one-photon annihilation; the annihilation via two virtual photons is suppressed by a factor $(\alpha/\alpha_s)^2$ [16, 17]. The charmoniumlike $X(3940)$ state was observed by Belle in the inclusive $e^+e^- \to J/\psi X$ spectrum and in the process $e^+e^- \to J/\psi D^*\bar{D}$ [19, 20], and the $X(4160)$ was observed in the process $e^+e^- \to J/\psi D^*\bar{D}^*$ [20]. Indications of a $D\bar{D}$ resonance in $e^+e^- \to J/\psi D\bar{D}$ were reported in Ref. [20]; however, the existence of this resonance could not be established reliably.

Here, we present an updated analysis of the process $e^+e^- \to J/\psi D\bar{D}$. The analysis is performed using the 980 fb^{-1} data sample collected by the Belle detector at the asymmetric-energy e^+e^- collider KEKB [21]. The data sample was collected at or near the $\Upsilon(1S)$, $\Upsilon(2S)$, $\Upsilon(3S)$, $\Upsilon(4S)$ and $\Upsilon(5S)$ resonances. The integrated luminosity is 1.4 times greater than the luminosity used in the previous analysis [20]. In addition, we use a multivariate method to improve the discrimination of the signal and background events and an amplitude analysis to study the J^{PC} quantum numbers of the $D\bar{D}$ system.

II. THE BELLE DETECTOR

The Belle detector is a large-solid-angle magnetic spectrometer that consists of a silicon vertex detector (SVD), a 50-layer central drift chamber (CDC), an array of aerogel threshold Cherenkov counters (ACC), a barrel-like arrangement of time-of-flight scintillation counters (TOF), and an electromagnetic calorimeter comprised of CsI(Tl) crystals (ECL) located inside a superconducting solenoid coil that provides a 1.5 T magnetic field. An iron flux-return located outside of the coil is instrumented to detect K^0_L mesons and to identify muons (KLM). The detector is described in detail elsewhere [22]. Two inner detector configurations were used. A 2.0 cm beampipe and a three-layer silicon vertex detector were used for the first sample of 156 fb^{-1}, while a 1.5 cm beampipe, a four-layer silicon detector and a small-cell inner drift chamber were used to record the remaining data [23].

We use a GEANT-based Monte Carlo (MC) simulation [24] to model the response of the detector, identify potential backgrounds and determine the acceptance. The MC simulation includes run-dependent detector performance variations and background conditions. The signal MC generation is described in Sec. IV.

III. RECONSTRUCTION

We select events of the type $e^+e^- \to J/\psi D\bar{D}$, where only the J/ψ and one of the D mesons are reconstructed; the other D meson is identified by the recoil mass of the $(J/\psi, D)$ system, which is denoted as $M_{\rm rec}$.

All tracks are required to originate from the interaction point region: we require $dr < 0.2$ cm and $|dz| < 2$ cm, where dr and dz are the cylindrical coordinates of the point of the closest approach of the track to the beam axis

(the z axis of the laboratory reference frame coincides with the positron-beam axis).

Charged π and K mesons are identified using likelihood ratios $R_{\pi/K} = \mathcal{L}_\pi/(\mathcal{L}_\pi + \mathcal{L}_K)$ and $R_{K/\pi} = \mathcal{L}_K/(\mathcal{L}_\pi+\mathcal{L}_K)$, where $\mathcal{L}_\pi$ and $\mathcal{L}_K$ are the likelihoods for π and K, respectively. The likelihoods are calculated from the combined time-of-flight information from the TOF, the number of photoelectrons from the ACC and dE/dx measurements in the CDC. We require $R_{K/\pi} > 0.6$ for K candidates and $R_{\pi/K} > 0.1$ for π candidates. The K (π) identification efficiency is typically 90% (98%) and the misidentification probability for non-K (-π) background is about 4% (30%).

Electron candidates are identified as CDC charged tracks that are matched to electromagnetic showers in the ECL. The track and ECL cluster matching quality, the ratio of the electromagnetic shower energy to the track momentum, the transverse shape of the shower, the ACC light yield and the track's dE/dx ionization are used in our electron identification selection criteria. A similar likelihood ratio is constructed: $R_e = \mathcal{L}_e/(\mathcal{L}_e+\mathcal{L}_h)$, where $\mathcal{L}_e$ and $\mathcal{L}_h$ are the likelihoods for electrons and charged hadrons (π, K and p), respectively [25]. An electron veto ($R_e < 0.9$) is imposed on π and K candidates. The veto rejects from 4 to 11% of background events, depending on the D decay channel, while its signal efficiency is more than 99%.

Muons are identified by their range and transverse scattering in the KLM. The muon likelihood ratio is defined as $R_\mu = \mathcal{L}_\mu/(\mathcal{L}_\mu + \mathcal{L}_\pi + \mathcal{L}_K)$, where $\mathcal{L}_\mu$ is the likelihood for muons [26].

The π^0 candidates are reconstructed via their decay to two photons; we require their energies to be greater than 30 MeV and their invariant mass $M_{\gamma\gamma}$ to satisfy $|M_{\gamma\gamma} - m_{\pi^0}| < 15$ MeV/c^2, where m_{π^0} is the nominal π^0 mass [6]. This requirement corresponds approximately to a 3σ mass window around the nominal mass.

Candidate K^0_S mesons are reconstructed from pairs of oppositely charged tracks (assumed to be pions) and selected on the basis of the $\pi^+\pi^-$ invariant mass, the candidate K^0_S momentum and decay angle, the inferred K^0_S flight distance in the xy plane, the angle between the K^0_S momentum and the direction from the interaction point to the K^0_S vertex, the shortest z distance between the two pion tracks, their radial impact parameters and numbers of hits in the SVD and CDC.

The J/ψ is reconstructed via its e^+e^- and $\mu^+\mu^-$ decay channels. For $J/\psi \to e^+e^-$ candidates, we include photons that have energies greater than 30 MeV and are within 50 mrad of a daughter lepton candidate momentum direction in the calculation of the J/ψ invariant mass. The J/ψ daughter leptons are identified as electrons or muons ($R_e > 0.1$ or $R_\mu > 0.1$) and not as kaons ($R_{K/e} < 0.9$ and $R_{K/\mu} < 0.9$ for the $J/\psi \to e^+e^-$ and $J/\psi \to \mu^+\mu^-$ decay modes, respectively). The combined lepton-pair identification efficiency is 91% and 75% and the fake rate is 0.07% and 0.13% for the $J/\psi \to e^+e^-$ and $J/\psi \to \mu^+\mu^-$ channel, respectively. We retain candidates that satisfy $|M_{J/\psi} - m_{J/\psi}| < 300$ MeV/c^2, where $M_{J/\psi}$ is the reconstructed mass and $m_{J/\psi}$ is the nominal mass [6]. The mass window is intentionally wide because this selection is at a preliminary stage and includes the events that will be used for the background determination.

The D^+ mesons are reconstructed in five decay channels: $K^0_S\pi^+$, $K^-\pi^+\pi^+$, $K^0_S\pi^+\pi^0$, $K^-\pi^+\pi^+\pi^0$, and $K^0_S\pi^+\pi^+\pi^-$. The D^0 mesons are reconstructed in four decay channels: $K^-\pi^+$, $K^0_S\pi^+\pi^-$, $K^-\pi^+\pi^0$, and $K^-\pi^+\pi^+\pi^-$. We retain candidates that satisfy -150 MeV/$c^2 < M_D - m_D < 350$ MeV/c^2, where M_D is the reconstructed mass and m_D is the nominal mass [6]. The mass window is chosen to be asymmetric to exclude peaking backgrounds from partially reconstructed multibody D decays, for example $D^0 \to K^-\pi^+\pi^0$ or $D^+ \to K^-\pi^+\pi^+$ backgrounds in the $D^0 \to K^-\pi^+$ event sample.

After the selection of the J/ψ and D candidates, we perform a mass-constrained fit to each candidate; then, the recoil mass $M_{\rm rec}$ is calculated. We retain the (J/ψ, D) pairs that satisfy $|M_{\rm rec} - m_D| < 350$ MeV/c^2. Finally, we perform a beam-constrained fit with $M_{\rm rec}$ constrained to the D mass to improve the $M_{D\bar{D}}$ resolution.

IV. MULTIVARIATE ANALYSIS AND GLOBAL OPTIMIZATION

A. Multivariate analysis

To improve the separation of signal and background events, we perform a multivariate analysis for each individual D decay channel followed by a global selection requirement optimization. For each D channel, the global optimization includes the definition of the signal region and the requirement on the multivariate-analysis output.

The algorithm used for the multivariate analysis is the multilayer perceptron (MLP) neural network implemented in the TMVA library [27]. For D decay channels without a daughter π^0, the neural network contains five variables: the cylindrical coordinate dr of the J/ψ vertex, the cylindrical coordinates dr and dz of the D vertex calculated relative to the J/ψ vertex (these coordinates being sensitive to the D flight distance), the angle between the D momentum and the direction from the J/ψ vertex to the D vertex, and the smaller of the two lepton-likelihood ratios R_e or R_μ of the J/ψ daughter leptons for the $J/\psi \to e^+e^-$ and $J/\psi \to \mu^+\mu^-$ channel, respectively. If the D meson has a daughter π^0, three additional π^0-related variables are used in the neural network: the minimum energy of the π^0 daughter photons in the laboratory reference frame, the π^0 mass, and the angle between $-\vec{p}_D$ and $\vec{p}_\gamma$, where $\vec{p}_D$ and $\vec{p}_\gamma$ are the momenta of the parent D and daughter γ in the π^0 rest frame.

The signal data sample consists of Monte-Carlo events generated by a combination of the PHOKHARA 9 [28] and EvtGen [29] generators. The PHOKHARA 9 gener-

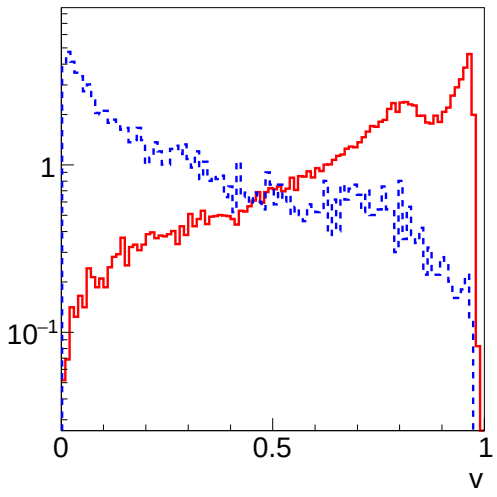

FIG. 1. Example of the MLP output (for the channel $D^0 \to K^-\pi^+\pi^0$). The red solid line is the MLP output for the signal events and the blue dashed line is the MLP output for the background events. Both distributions are normalized so that their integrals are equal to one.

ator generates the initial-state radiation photon(s); the remaining generation is performed by EvtGen. The background sample is taken from the data; a two-dimensional $(M_{J/\psi}, M_D)$ sideband is used. The background region includes all initially selected events except the events with $|M_{J/\psi} - m_{J/\psi}| < 100$ MeV/c^2 and $|M_D - m_D| < 50$ MeV/c^2. In addition, we select only the events with the $D\bar{D}$ invariant mass $M_{D\bar{D}} < 6$ GeV/c^2 for both signal and background samples. This requirement improves the signal and background separation, because the angle between the D momentum and the direction from the J/ψ vertex to the D vertex provides more effective separation for D mesons with larger momentum. The background data sample is split randomly into training and testing parts of equal size.

Example distributions of the MLP output v for the signal and background samples are shown in Fig. 1. The signal events tend to have a larger value of v, while the background events have smaller values of v. Thus, the requirements on the MLP output used in the global selection requirement optimization have the form $v > v_0$, where v_0 is a cutoff value.

B. Fit to the background

Before the global optimization, the events in the background region are fitted to estimate the expected number of the background events in the signal region. An unbinned maximum likelihood fit in the three-dimensional parameter space $\Phi_{\rm B} = (M_{J/\psi}, M_D, M_{\rm rec})$ is performed. The background density function is

$$\begin{aligned} B(\Phi_{\rm B}) =& P_2(\Phi_{\rm B})\exp(-\alpha M_{J/\psi}) \\ &+ R_{M_D}(M_D)P_1^D(M_{J/\psi}, M_{\rm rec}) \\ &+ R_{M_{J/\psi}}(\tilde{M}_{J/\psi})P_1^{J/\psi}(M_D, M_{\rm rec}), \end{aligned} \quad (1)$$

where P_2 is a three-dimensional second-order polynomial, P_1^D and $P_1^{J/\psi}$ are two-dimensional first-order polynomials, α is a rate parameter, R_{M_D} and $R_{M_{J/\psi}}$ are the resolutions in M_D and $M_{J/\psi}$, respectively, and $\tilde{M}_{J/\psi}$ is the scaled J/ψ mass:

$$\tilde{M}_{J/\psi} = m_{J/\psi} + \mathcal{S}(M_{J/\psi} - m_{J/\psi}), \quad (2)$$

where $\mathcal{S}$ is the scaling coefficient. This scaling accounts for the fact that the MC resolution in the J/ψ mass is significantly better than that measured with data. The resolutions are determined from a fit of the distributions of $M_{J/\psi}$ and M_D in the signal MC to a sum of an asymmetric Gaussian and asymmetric double-sided Crystal Ball functions [30]. Some of the coefficients of the polynomials are fixed at 0 for the D channels that have a small number of the background events. The average value of the J/ψ mass resolution scaling coefficient for all D channels is measured to be $\mathcal{S} = 0.79 \pm 0.02$. If the D mass resolution is scaled similarly to Eq. (2), the scaling coefficient depends on the D decay channel; it is possible to determine this coefficient from data only for channels with a large number of real D mesons in the background region: $D^+ \to K^-\pi^+\pi^+$ and $D^0 \to K^-\pi^+$. The resolutions in data and MC are found to be consistent for both $D^+ \to K^-\pi^+\pi^+$ and $D^0 \to K^-\pi^+$; thus, the resolution for the D mesons is not scaled. An example of the background fit results (for the channel $D^0 \to K^-\pi^+$) is shown in Fig. 2. The fit quality is estimated using the mixed-sample method [31]; the confidence levels are found to be not less than 15%.

C. Global selection requirement optimization

The global selection requirement optimization is performed by maximizing the value

$$\frac{\sum_i N_{\rm sig}^{(i)}}{\frac{a}{2} + \sqrt{\sum_i N_{\rm bg}^{(i)}}}, \quad (3)$$

where i is the index of the D decay channel, $N_{\rm sig}^{(i)}$ is the expected number of the signal events for the i-th channel, $N_{\rm bg}^{(i)}$ is the expected number of the background events in the signal region, and $a = 5$ is the target significance. This optimization method is based on Ref. [32]. The signal region is defined as

$$\left(\frac{M_{J/\psi} - m_{J/\psi}}{M_{J/\psi}^{(i)}}\right)^2 + \left(\frac{M_D - m_D}{M_D^{(i)}}\right)^2 < 1, \quad (4)$$

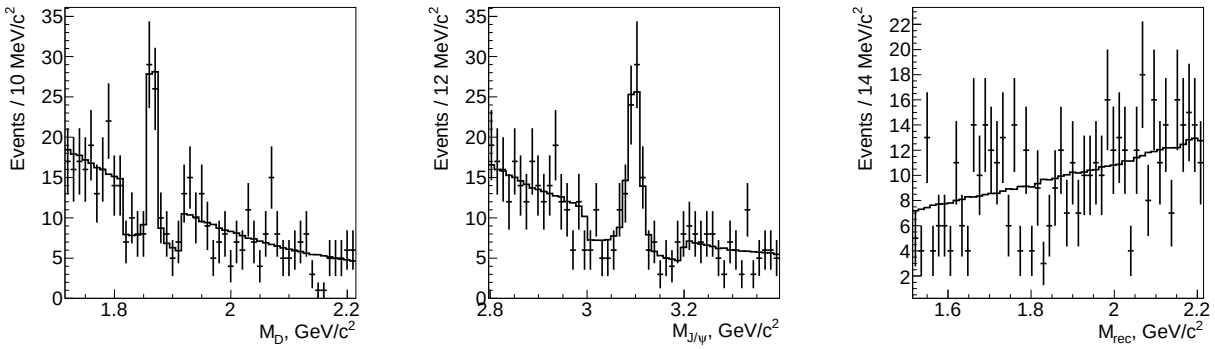

FIG. 2. Example of the results of the fit to the background events (for the channel $D^0 \to K^-\pi^+$). The points with error bars are the data and the solid line is the fit result. The region defined by $|M_{J/\psi} - m_{J/\psi}| < 100$ MeV/c^2, $|M_D - m_D| < 50$ MeV/c^2 [the region labeled (4) in Fig. 3] is excluded from the fit; because of this exclusion, the projections of both the data and the fit result onto M_D and $M_{J/\psi}$ have jump discontinuities.

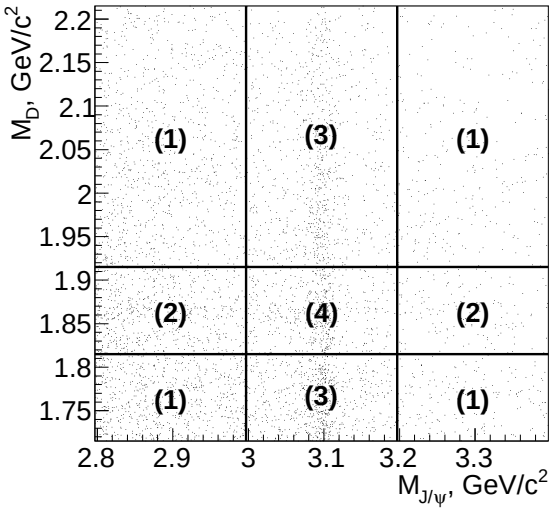

FIG. 3. Definition of the background subregions: (1) is the background region where both D and J/ψ mesons are fake, (2) is the real D region, (3) is the real J/ψ region. The central rectangle (4) is excluded from the background region as described in Sec. III.

$$\left|\frac{M_{\rm rec} - m_D}{M^{(i)}_{\rm rec}}\right| < 1, \tag{5}$$

where $M^{(i)}_{J/\psi}$ and $M^{(i)}_D$ are the half-axes of the signal region ellipse and $M^{(i)}_{\rm rec}$ is the half-width of the selected recoil mass region. All the values $M^{(i)}_{J/\psi}$, $M^{(i)}_D$ and $M^{(i)}_{\rm rec}$ are channel-dependent.

The expected number of signal events is given by

$$\begin{aligned} N^{(i)}_{\rm sig} =& \sigma^{(\mathrm{E}_\gamma<\mathrm{E}_{\rm cut})}_{e^+e^-\to J/\psi D\bar{D}}(\Upsilon(4S)) f^{(i)} \frac{N^{(i)}_{\rm rec}}{N^{(i)}_{(\Upsilon(4S)\ E_\gamma<E_{\rm cut})}} \\ & \times \mathcal{L}_{\Upsilon(4S)} \epsilon^{(i)}_S(v^{(i)}_0) \int\limits_{\rm SR} S^{(i)}(\Phi)\, d\Phi, \end{aligned} \tag{6}$$

where

$$\sigma^{(\mathrm{E}_\gamma<\mathrm{E}_{\rm cut})}_{e^+e^-\to J/\psi D\bar{D}} = \sigma^{(\rm Born)}_{e^+e^-\to J/\psi D\bar{D}} \frac{\sigma^{(E_\gamma<E_{\rm cut})}_{e^+e^-\to\mu^+\mu^-}}{\sigma^{(\rm Born)}_{e^+e^-\to\mu^+\mu^-}} \tag{7}$$

is the cross section of the process $e^+e^- \to J/\psi D\bar{D}(\gamma_{\rm ISR})(\gamma_{\rm ISR})$ with the condition that the photon(s) energy is less than the cutoff energy and the vacuum polarization taken into account, $\sigma^{(\rm Born)}_{\rm process}$ is the Born cross section of the specified process, $f^{(i)}$ is the fraction of i-th channel, $N^{(i)}_{(\Upsilon(4S)\ E_\gamma<E_{\rm cut})}$ is the number of generated MC events at the $\Upsilon(4S)$ resonance with $E_\gamma < E_{\rm cut}$, $N^{(i)}_{\rm rec}$ is the total number of reconstructed MC events for all beam energies, $\mathcal{L}_{\Upsilon(4S)}$ is the integrated luminosity at the $\Upsilon(4S)$ resonance, $\epsilon^{(i)}_S(v^{(i)}_0)$ is the efficiency of the requirement ($v > v^{(i)}_0$) on the MLP output v for the signal events, SR is the signal region, and $S^{(i)}(\Phi)$ is the signal probability density function (PDF), which is proportional to the product of the resolutions in M_D, $M_{J/\psi}$ and $M_{\rm rec}$. The factor $N^{(i)}_{\rm rec}/N^{(i)}_{(\Upsilon(4S)\ E_\gamma<E_{\rm cut})}$ is the reconstruction efficiency corrected for the difference between the full cross section and $\sigma^{(\mathrm{E}_\gamma<\mathrm{E}_{\rm cut})}_{e^+e^-\to J/\psi D\bar{D}}$ and for the difference between the number of events for all beam energies and at the $\Upsilon(4S)$ resonance. The ratio $\sigma^{(E_\gamma<E_{\rm cut})}_{\mu^+\mu^-}(\Upsilon(4S))/\sigma^{(\rm Born)}_{\mu^+\mu^-}(\Upsilon(4S))$ is taken from Ref. [33]. The ratio $N^{(i)}_{(\Upsilon(4S)\ E_\gamma<E_{\rm cut})} \times \sigma^{(\rm Born)}_{e^+e^-\to\mu^+\mu^-}(\Upsilon(4S))/\sigma^{(E_\gamma<E_{\rm cut})}_{e^+e^-\to\mu^+\mu^-}(\Upsilon(4S))$ does not

depend on the cutoff energy; it is determined from a fit to its dependence on $E_{\rm cut}$ in the range between 20 and 100 MeV.

The background can be subdivided into three classes of events: those with real D mesons, those with real J/ψ mesons, and a featureless combinatorial background. These components can have a different efficiency dependence on the MLP output cutoff value $v_0^{(i)}$ as well as different distributions in $M_{D\bar{D}}$ and angular variables. To account for these differences, the background region is divided into three parts with definition indicated in Fig. 3. The expected number of the background events is

$$N_{\rm bg}^{(i)} = \begin{pmatrix} I_{\rm sm}^{\rm (SR)} \\ I_D^{\rm (SR)} \\ I_{J/\psi}^{\rm (SR)} \end{pmatrix}^T \begin{pmatrix} I_{\rm sm}^{(1)} & I_D^{(1)} & I_{J/\psi}^{(1)} \\ I_{\rm sm}^{(2)} & I_D^{(2)} & I_{J/\psi}^{(2)} \\ I_{\rm sm}^{(3)} & I_D^{(3)} & I_{J/\psi}^{(3)} \end{pmatrix}^{-1} \times \begin{pmatrix} \epsilon_B^{(1)}(v_0^{(i)}) N_{\rm (bg\ rec)}^{(i)(1)} \\ \epsilon_B^{(2)}(v_0^{(i)}) N_{\rm (bg\ rec)}^{(i)(2)} \\ \epsilon_B^{(3)}(v_0^{(i)}) N_{\rm (bg\ rec)}^{(i)(3)} \end{pmatrix}. \quad (8)$$

where each I is a background distribution integral with the superscript defining the subregion and the subscript identifying the background component, $N_{\rm (bg\ rec)}^{(i)(j)}$ is the number of reconstructed data events in the j-th background subregion, and $\epsilon_B^{\rm (j)}(v_0^{(i)})$ is the efficiency of the requirement on the MLP output for the background events in the j-th background subregion.

Four parameters per D channel are determined from the global selection requirement optimization. They include the definition of the signal region ($M_{J/\psi}^{(i)}$, $M_D^{(i)}$ and $M_{\rm rec}^{(i)}$) and the MLP output cutoff value $v_0^{(i)}$. The MLP output requirement is not used for the two low-background D decay channels ($D^+ \to K^-\pi^+\pi^+$ and $D^0 \to K^-\pi^+$) because it has no effect.

The resulting signal region definition parameters vary in the range $33-65$ MeV/c^2, $8-17$ MeV/c^2 and $38-57$ MeV/c^2 for $M_{J/\psi}^{(i)}$, $M_D^{(i)}$ and $M_{\rm rec}^{(i)}$, respectively. The finally selected data sample contains $N_{\rm obs} = 103$ events.

After the global optimization, the background fits are performed again; only events passing the resulting MLP output selection requirement $v > v_0^{(i)}$ are used. The weights of the background events for all D channels are determined as the coefficients of the numbers of background events in the corresponding background region in Eq. (8) (since the MLP output requirement has already been applied, $\epsilon_B^{\rm (j)}(v_0^{(i)}) = 1$). The background event weights are then used to calculate the background distribution in $M_{\rm rec}$. The resulting $M_{\rm rec}$ signal and background distributions are shown in Fig. 4.

The expected number of background events in the signal region is $N_{\rm bg} = 24.9 \pm 1.1 \pm 1.6$. The statistical error is calculated from the event weights; it is found to be 4.5%. The systematic error is determined to be 6.3% and it includes the error due to the difference of the expected number of the background events in the training and testing samples and the statistical error of the background PDF. The overall error, including both statistical and systematic errors, is 7.7%. The expected fraction of the background events in the signal region is $b_0 = N_{\rm bg}/N_{\rm obs} = 0.24 \pm 0.03$.

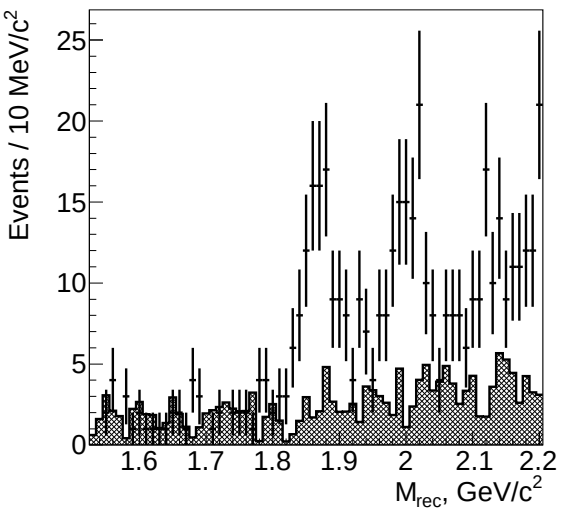

FIG. 4. The signal and background distributions in $M_{\rm rec}$. The points with error bars are the data with the channel-dependent signal region selection requirements defined by Eq. (4) and MLP output requirements applied. The hatched histogram is the background. Note that the definition of the signal region $M_{\rm rec}$ requirement depends on the D decay channel.

V. AMPLITUDE ANALYSIS FORMALISM

We perform an amplitude analysis in a six-dimensional parameter space

$$\Phi = (M_{D\bar{D}}, \theta_{\rm prod}, \theta_{J/\psi}, \theta_{X^*}, \varphi_{\ell^-}, \varphi_D), \quad (9)$$

where $\theta_{\rm prod}$ is the production angle, $\theta_{J/\psi}$ and θ_{X^*} are the J/ψ and X^* helicity angles, respectively, and φ_{ℓ^-} and φ_D are the ℓ^- and D azimuthal angles, respectively. The exact definitions of the angles are given in Appendix A. In general, the number of dimensions for the process $e^+e^- \to \ell^+\ell^- D\bar{D}$ is

$$3N_f - N_c - N_r = 7, \quad (10)$$

where $N_f = 4$ is the number of the final state particles, $N_c = 4$ is the number of conservation relations and $N_r = 1$ is the number of rotations around the beam axis. Since the leptons are produced in the decay of the narrow J/ψ state, their invariant mass can be ignored, thereby reducing the number of dimensions by one.

The amplitude of the process $e^+e^- \to J/\psi D\bar{D}$ is represented by a sum of individual contributions. The default amplitude model includes a nonresonant amplitude and a new resonance X^* in the $D\bar{D}$ system with $J^{PC} = 0^{++}$ or 2^{++}. Since the X^* is a resonance in the $D\bar{D}$ system, its quantum numbers are in the "normal" series [$P = (-1)^J$]; thus, the asterisk is added, as for the mesons with open flavor. In the case of one-photon production, odd values of the X^* spin are forbidden by C-parity conservation because the $D\bar{D}$ pair has $C = (-1)^{J(X^*)}$.

The X^* signal is described by the Breit-Wigner amplitude:

$$A_{X^*}(M) = \left(\frac{p(M)}{p(m)}\right)^L \frac{F_L(M)}{m^2 - M^2 - im\Gamma(M)}, \qquad (11)$$

where m is the resonance mass, M is the invariant mass of its daughters, $p(M)$ is the momentum of a daughter particle in the rest frame of the mother particle calculated at the mother's mass M, L is the decay angular momentum, $F_L(M)$ is the Blatt-Weisskopf form factor and $\Gamma(M)$ is the mass-dependent width. The Blatt-Weisskopf form factor is given by [34]

$$\begin{aligned} F_0(M) &= 1, \\ F_2(M) &= \sqrt{\frac{z_0^2 + 3z_0 + 9}{z^9 + 3z + 9}}, \end{aligned} \qquad (12)$$

where $z = (p(M)r)^2$ (r being the hadron scale), and $z_0 = (p(m)r)^2$. The mass-dependent width is given by

$$\Gamma(M) = \Gamma\left(\frac{p(M)}{p(m)}\right)^{2L+1} \frac{m}{M} F_L^2(M), \qquad (13)$$

where Γ is the resonance width.

The nonresonant amplitude is given by

$$A_{\rm NR}(M_{D\bar{D}}) = \sqrt{F_{D\bar{D}}(M_{D\bar{D}})}, \qquad (14)$$

where $F_{D\bar{D}}(M)$ is the nonresonant-amplitude form factor. Three different parameterizations are used for $F_{D\bar{D}}(M)$. The default choice is a constant nonresonant amplitude:

$$F_{D\bar{D}}(M_{D\bar{D}}) = 1. \qquad (15)$$

Another parameterization is based on Ref. [35]. The matrix element for the process $e^+e^- \to \psi\chi_c$ is integrated over angle, and $M_{D\bar{D}}$ is used instead of the χ_c mass. The result is

$$\begin{aligned} F_{D\bar{D}}(M_{D\bar{D}}) = \frac{2048}{3s^7m_c^2}\big[&180224m_c^{10} + 149504m_c^8 A \\ &+ m_c^6(44928A^2 + \frac{1792}{3}B) \\ &+ m_c^4(5376A^3 + \frac{928}{3}AB) \\ &+ m_c^2(222A^4 + 34A^2B) \\ &+ (\frac{A^5}{2} - \frac{A^3B}{6})\big], \end{aligned} \qquad (16)$$

where

$$A = m_{J/\psi}^2 + M_{D\bar{D}}^2 - s \qquad (17)$$

and

$$B = s^2 - 2s(m_{J/\psi}^2 + M_{D\bar{D}}^2) + (m_{J/\psi}^2 - M_{D\bar{D}}^2)^2 \qquad (18)$$

with $\sqrt{s} = m_{\Upsilon(4S)}$ and $m_c = 1.5$ GeV/c^2. This nonresonant amplitude model is denoted hereinafter as the NRQCD model (although, for the actual NRQCD calculation of the $e^+e^- \to \psi\chi_c$ cross section, the χ_c mass is set to $2m_c$ [35]).

The third parameterization is based on Ref. [36]. The matrix element for the process $e^+e^- \to J/\psi D\bar{D}$ is proportional to $M_{D\bar{D}}^{-4}$ for $4m_D^2 \ll M_{D\bar{D}}^2 \ll s$; this dependence is used for the entire fitting region:

$$F_{D\bar{D}}(M_{D\bar{D}}) = \frac{1}{M_{D\bar{D}}^4}. \qquad (19)$$

This amplitude model is identified below as the $M_{D\bar{D}}^{-4}$ nonresonant amplitude.

In the determination of systematic errors, we also use a model without a nonresonant contribution but with an additional form factor for the resonant amplitude [37]:

$$A_{X^*}(M) \to A_{X^*}(M)[1 + \beta(M_{D\bar{D}} - 2m_{D^0})], \qquad (20)$$

where β is a form-factor parameter.

The angle-dependent part of the amplitude is calculated using the helicity formalism (see Appendix A); the result is

$$\begin{aligned} &A_{\lambda_{\rm beam}\,\lambda_{J/\psi}\,\lambda_{X^*}\,\lambda_{\ell\ell}}(\Phi) \\ &\quad = H_{\lambda_{J/\psi}\,\lambda_{X^*}}\, d^1_{\lambda_{\rm beam}\,\lambda_{J/\psi} - \lambda_{X^*}}(\theta_{\rm prod}) e^{i\lambda_{J/\psi}\varphi_{\ell^-}} \\ &\qquad \times d^1_{\lambda_{J/\psi}\,\lambda_{\ell\ell}}(\theta_{J/\psi}) e^{i\lambda_{X^*}\varphi_D} d^{J(X^*)}_{\lambda_{X^*}\,0}(\theta_{X^*}), \end{aligned} \qquad (21)$$

and

$$A_{\lambda_{\rm beam}\,\lambda_{\ell\ell}}(\Phi) = \sum_{\substack{\lambda_{J/\psi}=-1,0,1 \\ \lambda_X=-J(X),\ldots,J(X)}} A_{\lambda_{\rm beam}\,\lambda_{J/\psi}\,\lambda_{X^*}\,\lambda_{\ell\ell}}(\Phi) \qquad (22)$$

where $H_{\lambda_{J/\psi}\,\lambda_{X^*}}$ is the production helicity amplitude, $d^j_{m_1\,m_2}(\theta)$ are Wigner d-functions, λ is the helicity of the particle specified by the index, $\lambda_{\rm beam}$ is the sum of helicities of the beam electron and positron and $\lambda_{\ell\ell}$ is the sum of helicities of the J/ψ decay products.

The signal density function is

$$S(\Phi) = \sum_{\substack{\lambda_{\rm beam}=-1,1 \\ \lambda_{\ell\ell}=-1,1}} \Big| \sum_{X^*} A_{\lambda_{\rm beam}\,\lambda_{\ell\ell}}(\Phi) A_{X^*}(M_{D\bar{D}}) \Big|^2, \qquad (23)$$

where X^* is any contribution to the signal (X^* resonance or nonresonant amplitude). The resolution in $M_{D\bar{D}}$ may be taken into account by substituting

$$\begin{aligned} S(\Phi) \to \sum_{i_g=-n_g}^{n_g} &R_{M_{D\bar{D}}}(M_{D\bar{D}}, i_g\Delta M_{D\bar{D}})\Delta M_{D\bar{D}} \\ &\times S(M_{D\bar{D}} + i_g\Delta M_{D\bar{D}}, \ldots), \end{aligned} \qquad (24)$$

where $R_{M_{D\bar{D}}}$ is the resolution in $M_{D\bar{D}}$, $\Delta M_{D\bar{D}}$ is the distance between grid points and i_g is the grid point index. The resolution in $M_{D\bar{D}}$ is $\sim$12 MeV/c^2 for $M_{D\bar{D}}$ range between 5 and 6 GeV/c^2; it is smaller for lower $D\bar{D}$ masses. The resolution is much smaller than the width of the $M_{D\bar{D}}$ structure (see Fig. 6) and can be ignored for the default fit; nevertheless, it is taken into account since alternative models with relatively narrow states $X(3915)$ or $\chi_{c2}(2P)$ are considered.

The construction of the likelihood function follows Ref. [38]. The function to be minimized is

$$F = -2\sum_k \ln\Big((1-b)\frac{S(\Phi_k)}{\sum\limits_l S(\Phi_l)} + b\frac{B(\Phi_k)}{\sum\limits_l B(\Phi_l)}\Big) + \frac{(b-b_0)^2}{\sigma_{b_0}^2}, \tag{25}$$

where b is the fraction of the background events, $B(\Phi)$ is the background density in the signal region determined from the fit to the background, b_0 is the expected background fraction and $\sigma_{b_0}^2$ is its error. The index k runs over data events; the index l runs over MC events generated uniformly over the phase space and reconstructed using the same selection requirements as in data. This procedure takes into account the nonuniformity of the reconstruction efficiency but requires a parameterization of the background shape. For the background, the likelihood is

$$F = -2\sum_k w_k \ln\Big(\frac{B(\Phi_k)}{\sum\limits_l B(\Phi_l)}\Big), \tag{26}$$

where w_k is the weight of the k-th background event, calculated as described in Sec. IV C.

VI. FIT TO THE DATA

A. Fit to the background

The background density function is given by

$$B(\Phi) = \frac{P_2(\Phi)\left(\exp(-\xi[p(M_{D\bar{D}})]^2) + \eta\right)[p(M_{D\bar{D}})]^{-\zeta}}{[1-u_1(\cos^2\theta_{\rm prod})^{v_1}][1-u_2(\cos^2\theta_{J/\psi})^{v_2}]}, \tag{27}$$

where $P_2(\Phi)$ is a six-dimensional second-order polynomial and u_1, u_2, v_1, v_2, ξ, η and ζ are coefficients. The projections of the fit results onto the individual variables are shown in Fig. 5.

B. Fit to the signal

The result of the fit to the signal events in the default model are listed in Table I for two X^* quantum-number hypotheses: $J^{PC} = 0^{++}$ and $J^{PC} = 2^{++}$. There are three solutions for the 2^{++} hypothesis; all solutions have very similar likelihood values ($|\Delta(-2\ln L)| < 1$). A significant resonance is observed for both the 0^{++} and 2^{++} hypotheses; the 0^{++} hypothesis is preferred. The significance is calculated using Wilks' theorem [39] with six and twelve degrees of freedom for the 0^{++} and 2^{++} hypotheses, respectively. The global significance calculated using the method described in Ref. [40] is 8.5σ for the 0^{++} hypothesis. Thus, we observe a new charmoniumlike state that is referred to hereinafter as the $X^*(3860)$. The projections of the fit results onto $M_{D\bar{D}}$ and the angular variables for the case of the $X^*(3860)$ with $J^{PC} = 0^{++}$ are shown in Fig. 6 and the amplitudes are shown in Table II. The helicity amplitudes $H_{1\,0}$ and $H_{0\,0}$ almost exactly coincide (with large error). This is consistent with pure S-wave production of the $X^*(3860)$ [see Eq. (A15)].

TABLE I. Fit results in the default model (constant nonresonant amplitude). For the 2^{++} hypothesis, there are three solutions.

J^{PC}	Mass, MeV/c^2	Width, MeV	Significance
0^{++}	3862^{+26}_{-32}	201^{+154}_{-67}	9.1σ
2^{++}	3879^{+20}_{-17}	171^{+129}_{-62}	8.0σ
2^{++}	3879^{+17}_{-17}	148^{+108}_{-50}	8.0σ
2^{++}	3883^{+26}_{-24}	227^{+201}_{-125}	8.0σ

TABLE II. The $X^*(3860)$ ($J^{PC} = 0^{++}$) amplitudes in the default model.

Amplitude	Value
$\Re H_{0\,0}$	1 (fixed)
$\Im H_{0\,0}$	0 (fixed)
$\Re H_{1\,0}$	1.00 ± 0.38
$\Im H_{1\,0}$	0.01 ± 0.93

Other known states with $J^{PC} = 0^{++}$ or 2^{++} may also contribute to this process. We consider the states with mass $\sim$3.9 GeV/c^2 [$X(3915)$ and $\chi_{c2}(2P)$] and the states observed in double-charmonium production [$X(3940)$ and $X(4160)$]. Note that the $X(3940)$ decays to $D^*\bar{D}$ [19, 20] and it consequently may be observed in the process $e^+e^- \to J/\psi D\bar{D}$ only if its quantum numbers are $J^{PC} = 2^{++}$. As in Ref. [20], because of low statistics we do not consider the possibility that the $X^*(3860)$ peak is due to more than one state. We check whether the $X^*(3860)$ is compatible with the states listed above by performing a fit with Gaussian constraints to the known resonance parameters [6] on the X^* mass and width. For known states with $J^{PC} = 2^{++}$, the exclusion levels are calculated from MC pseudoexperiments similarly to the comparison of $J^{PC} = 0^{++}$ and 2^{++} hypotheses described in Sec. VI D; for 0^{++} states, the exclusion levels are calculated as $\sqrt{\Delta(-2\ln L)}$. The calculation is performed for all nonresonant amplitude models. The results are listed in Table III. The $X(3915)$ is excluded at 3.3σ and 4.9σ in the case of $J^{PC} = 0^{++}$ and 2^{++}, respectively. Other known states are excluded at more than 5σ. In addition, we compare the $X^*(3860)$ and the lattice prediction for the $\chi_{c0}(2P)$ provided in Ref. [41]. The parameters

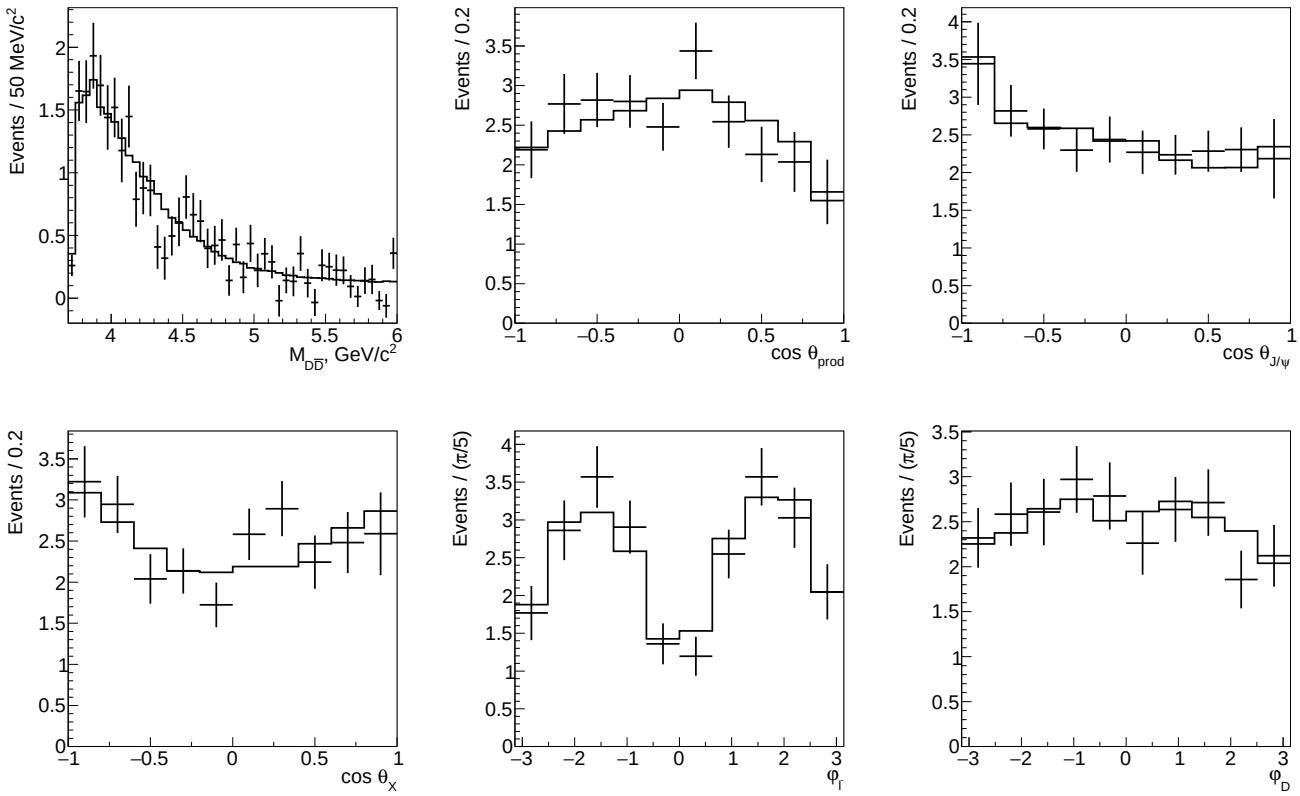

FIG. 5. Projections of the background fit results onto $M_{D\bar{D}}$ and angular variables. The points with error bars are data and the solid line is the fit result.

TABLE III. Comparison of the $X^*(3860)$ and known charmoniumlike states: exclusion levels for the hypotheses of the $X^*(3860)$ being the indicated state for different nonresonant amplitude models.

State	J^{PC}	Nonresonant amplitude		
		Constant	NRQCD	M_{DD}^{-4}
$X(3915)$	0^{++}	5.2σ	4.3σ	3.3σ
$X(3915)$	2^{++}	6.1σ	6.1σ	4.9σ
$\chi_{c2}(2P)$	2^{++}	6.8σ	7.0σ	6.2σ
$X(3940)$	2^{++}	6.0σ	5.6σ	5.2σ
$X(4160)$	0^{++}	6.8σ	6.3σ	5.8σ
$X(4160)$	2^{++}	10.7σ	11.0σ	13.5σ
$\chi_{c0}(2P)$ (lattice)	0^{++}	4.3σ	3.6σ	2.7σ

$M = 3966 \pm 20$ MeV/c^2 and $\Gamma = 67 \pm 18$ MeV are used. The comparison is performed in the same way as those for the experimentally known states with $J^{PC} = 0^{++}$; the results are shown in Table III. The difference of the $X^*(3860)$ and predicted $\chi_{c0}(2P)$ parameters is at 2.7σ level. Note that the systematic errors have not been determined in Ref. [41]; thus, the actual level of disagreement should be less than 2.7σ.

C. Systematic uncertainties

The systematic uncertainties of the $X^*(3860)$ mass and width are listed in Table IV. One source of mass and width systematic error is the systematic uncertainty due to the nonresonant amplitude model dependence. We perform a fit with all nonresonant amplitude models and consider the maximal variations of the $X^*(3860)$ mass and width as the systematic uncertainty. Note that there are two solutions for both fits with the NRQCD and $M_{D\bar{D}}^{-4}$ nonresonant amplitudes in the case of $J^{PC} = 0^{++}$; all solutions are included into the calculation of the maximal variations. The systematic error related to the alternative signal model defined in Eq. (20) is included separately.

A different fit-related systematic uncertainty source is the fit bias. The fit bias is estimated from the mass and width distributions in MC pseudoexperiments generated in accordance with the default fit result. We find that the position of the peak of the mass distribution is in good agreement with the fit result in data, while the position of the peak of the width distribution is shifted from the value in data. Thus, a fit bias uncertainty is assigned only to the $X^*(3860)$ width.

Another systematic uncertainty source considered in

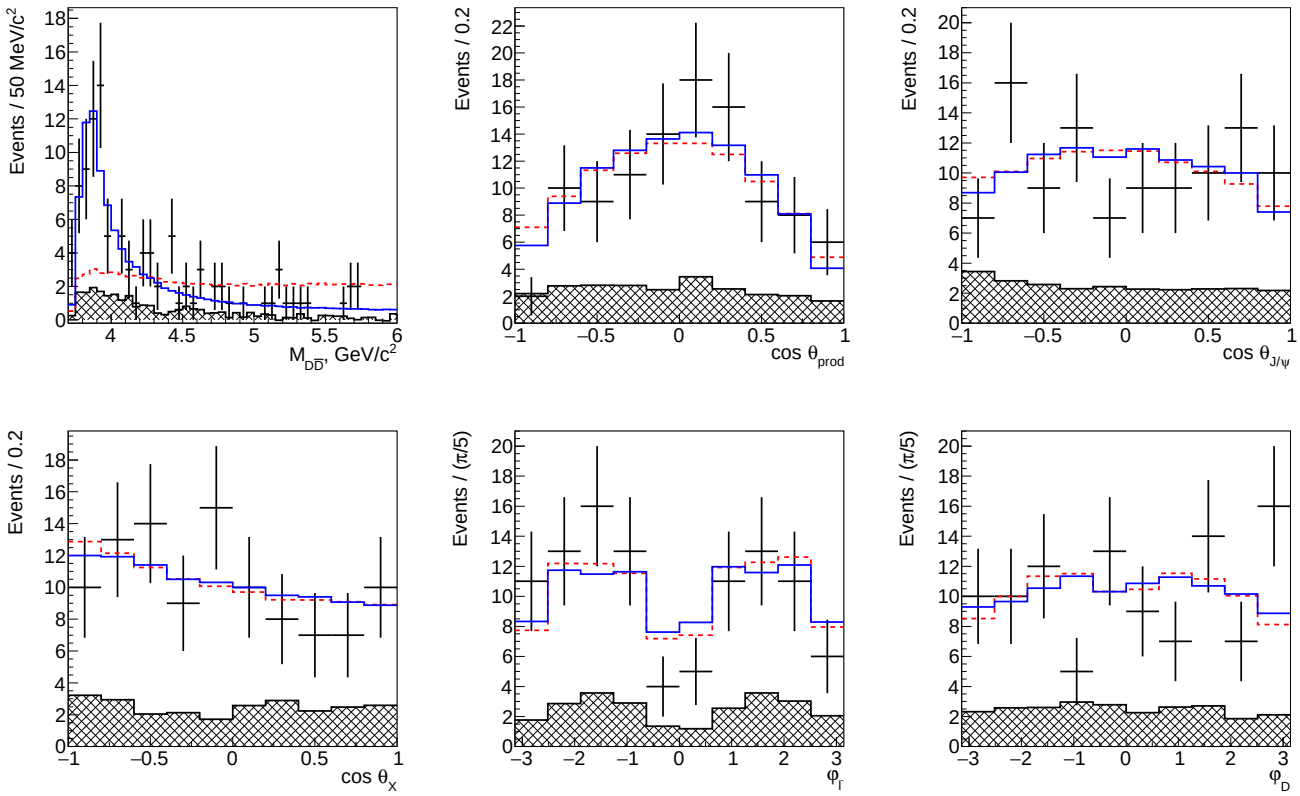

FIG. 6. Projections of the signal fit results in the default model onto $M_{D\bar{D}}$ and angular variables. The points with error bars are the data, the hatched histograms are the background, the blue solid line is the fit with a new X^* resonance ($J^{PC} = 0^{++}$) and the red dashed line is the fit with nonresonant amplitude only.

TABLE IV. Systematic errors for the $X^*(3860)$ mass (in MeV/c^2) and width (in MeV).

Error source	Mass	Width
Nonresonant amplitude model	$^{+40.2}_{-0.0}$	$^{+0.0}_{-82.0}$
Signal model	$^{+0.0}_{-10.2}$	$^{+0.0}_{-4.0}$
Fit bias	—	$^{+32.6}_{-0}$
Optimization	$^{+0.0}_{-3.1}$	$^{+71.1}_{-0.0}$
Background mass calculation	$^{+0.0}_{-7.9}$	$^{+40.0}_{-0.0}$
D mass	± 0.2	—
Total	$^{+40.2}_{-13.3}$	$^{+87.9}_{-82.1}$

the previous analysis [20] is the variation of selection requirements. There is no straightforward analog of this uncertainty in the new analysis because of the complex selection optimization procedure. However, its last stage (the global optimization) can be varied. We change the target significance a in Eq. (3) from its default value (5) by ± 1 unit, repeat the global optimization and fitting with the new target significance and treat the variations of the $X^*(3860)$ mass and width as the systematic uncertainty related to the optimization.

The default $M_{D\bar{D}}$ calculation procedure for the background events is the same as for the events in the signal region. We perform a mass-constrained fit to the J/ψ and D candidates with the candidate mass fixed at $m_{J/\psi}$ and m_D, respectively. Alternatively, the background region is divided into smaller rectangular $(M_{J/\psi}, M_D)$ subregions. The candidate mass is fixed at the center of its subregion. After the fit with $M_{\rm rec}$ constrained to m_D, the resulting value of $m_{D\bar{D}}$ is shifted in such a way that the threshold of the new distribution is at $2m_D$. The background distribution is then calculated in the same way as for the default mass calculation method; the difference in the fit results is considered as the background mass calculation method systematic uncertainty.

The mass also has a systematic error due to the uncertainty in the mass of the $X^*(3860)$ decay products (the D mesons).

The $X^*(3860)$ global significance for alternative models is shown in Table V. The minimal global significance of the $X^*(3860)$ is found to be 6.5σ. Thus, the new state $X^*(3860)$ is clearly observed, accounting for both statistical and systematic uncertainties.

TABLE V. The $X^*(3860)$ global significance for alternative models.

Model	Significance
Default (constant nonresonant)	8.5σ
NRQCD nonresonant	7.6σ
$M_{D\bar{D}}^{-4}$ nonresonant	6.5σ
Background mass calculation	8.4σ
Optimization ($a = 4$)	8.1σ
Optimization ($a = 6$)	8.1σ

D. Comparison of J^{PC} hypotheses

The $X^*(3860)$ quantum number hypotheses $J^{PC} = 0^{++}$ and 2^{++} are compared using MC simulation. We generate MC pseudoexperiments in accordance with the fit result with the 2^{++} $X^*(3860)$ signal in data and fit them with the 2^{++} and 0^{++} signals. The resulting distribution of $\Delta(-2\ln L) = (-2\ln L)_{J^{PC}=2^{++}} - (-2\ln L)_{J^{PC}=0^{++}}$ is fitted to an asymmetric Gaussian function and the p-value is calculated as the integral of the fitting function normalized to 1 from the value of $\Delta(-2\ln L)$ in data to $+\infty$. If there are multiple solutions for the 2^{++} hypothesis in data (this is the case for the default model), then the exclusion level depends on the solution. The exclusion level calculation is performed for all solutions. The comparison the $X^*(3860)$ quantum number hypotheses includes an additional model, where the Blatt-Weisskopf form factor hadron scale r is allowed to vary between 0 and 10 GeV^{-1} (this model is not included in the calculation of the systematic errors of the $X^*(3860)$ mass and width because, for the preferred hypothesis $J^{PC} = 0^{++}$, the Blatt-Weisskopf form factor is $F_0 = 1$). The results are presented in Table VI. The $J^{PC} = 0^{++}$ hypothesis is favored over the 2^{++} hypothesis at the level of 2.5σ.

We also generate MC pseudoexperiments in accordance with the fit results for the 0^{++} hypothesis and obtain the distribution of $\Delta(-2\ln L)$. This distribution is fitted to an asymmetric Gaussian function and the confidence level of the 0^{++} hypothesis is calculated as the integral of the fitting function normalized to 1 from $-\infty$ to the value of $\Delta(-2\ln L)$ in data. The resulting confidence levels are shown in Table VI. The distributions of $\Delta(-2\ln L)$ for the default model are shown in Fig. 7.

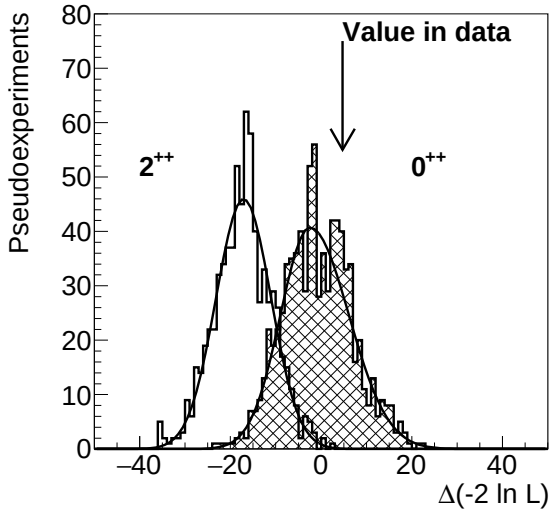

FIG. 7. Comparison of the 0^{++} and 2^{++} hypotheses in the default model (constant nonresonant amplitude). The histograms are distributions of $\Delta(-2\ln L)$ in MC pseudoexperiments generated in accordance with the fit results with 2^{++} (open histogram) and 0^{++} (hatched histogram) signals. The 2^{++} pseudoexperiments are generated for the second solution (see Table I), which has a minimal exclusion level of 3.8σ. The $\Delta(-2\ln L)$ value observed in data (4.8) is indicated with an arrow.

TABLE VI. Exclusion levels of the 2^{++} hypothesis and confidence levels of the 0^{++} hypothesis. If there are multiple solutions, the results for the solution with the smallest exclusion level are shown.

Model	2^{++} exclusion	0^{++} CL
Default (constant nonresonant)	3.8σ	77%
NRQCD nonresonant	3.4σ	73%
$M_{D\bar{D}}^{-4}$ nonresonant	3.6σ	70%
Background mass calculation	3.8σ	75%
Optimization ($a = 4$)	3.3σ	69%
Optimization ($a = 6$)	3.4σ	64%
Free r	2.5σ	74%

E. Cross section

The cross section calculation is similar to that used in the previous analyses [19, 20]. The full cross section can be calculated from Eq. (6) summed over all D decay channels with the efficiency corrected by weighting generated and reconstructed events in accordance with the measured signal PDF. The cross section for the process $e^+e^- \to J/\psi X^*(3860)(\to D\bar{D})$ includes the $X^*(3860)$ fit fraction, which is calculated as $\int S_{X^*(3860)}(\Phi)d\Phi / \int S(\Phi)d\Phi$, where $S_{X^*(3860)}(\Phi)$ is the signal PDF with the $S_{X^*(3860)}(\Phi)$ contribution only. The cross sections are calculated at all energy points with results listed in Table VII.

The cross section is corrected for differences between the particle identification requirement efficiencies in data and MC, which are obtained from a $D^{*+} \to D^0(\to K^-\pi^+)\pi^+$ control sample for K and π and a sample of $\gamma\gamma \to \ell^+\ell^-$ events for μ and e. The ratio of the particle identification efficiency in data and MC averaged over all D decay channels is $(92.4 \pm 4.1)\%$.

The cross section is also corrected for differences be-

TABLE VII. Born cross section measurement results.

Data set	Energy, GeV	$\sigma^{(\mathrm{Born})}_{e^+e^-\to J/\psi X^*(3860)(\to D\bar{D})}$, fb
$\Upsilon(1S)$	9.46	$77^{+66\,+9}_{-66\,-7}$
$\Upsilon(2S)$	10.02	$6.9^{+12.6\,+0.9}_{-12.6\,-0.7}$
$\Upsilon(3S)$	10.36	$77^{+85\,+11}_{-85\,\,-8}$
Continuum	10.52	$5.5^{+5.7\,+0.7}_{-5.7\,-0.5}$
$\Upsilon(4S)$	10.58	$21.7^{+3.9\,+2.9}_{-4.3\,-2.1}$
$\Upsilon(5S)$	10.87	$17.9^{+7.2\,+2.4}_{-7.3\,-1.8}$

tween the K^0_S and π^0 reconstruction efficiencies in data and MC. The K^0_S efficiency correction is determined from a sample of $D^0 \to K^0_S\pi^+\pi^-$ decays. The efficiency ratio is $(99.1 \pm 2.3)\%$ for the channel $D^0 \to K^0_S\pi^+\pi^-$ and is slightly different for other channels with a daughter K^0_S because of the different K^0_S momentum distribution. The average K^0_S efficiency ratio is $(99.8 \pm 0.4)\%$. This ratio, as well as the average π^0 efficiency ratio described below, is closer to 100% and has a small error since only some D decay channels have a daughter K^0_S or π^0.

The π^0 efficiency correction is determined from a $\tau^- \to \pi^-\pi^0\nu_\tau$ control sample [42]. Note that the resulting correction differs from the result of Ref. [42] because the π^0 momentum distributions of the π^0 in individual D decay channels differ from the momentum distribution in Ref. [42]. For example, the efficiency ratio is $(95.9\pm2.2)\%$ for the channel $D^0 \to K^-\pi^+\pi^0$. The average π^0 efficiency ratio in data and MC is $(99.3 \pm 0.4)\%$.

The systematic error sources are listed in Table VIII. Some of these are the same as for the $X^*(3860)$ mass and width. They include the nonresonant amplitude model dependence, the optimization variation and the background mass calculation uncertainty. The uncertainty related to the alternative signal model defined in Eq. (20) is not included since this model does not distinguish the resonant and nonresonant contributions. Other systematic error sources include the efficiency difference between the training and testing signal samples, uncertainties due to the statistical errors of the signal PDF parameters, luminosity, track reconstruction, J/ψ and D branching fractions and corrections due to the differences between the efficiency in data and MC for particle identification requirements and K^0_S and π^0 reconstruction efficiencies.

TABLE VIII. Relative systematic errors of the Born cross section for $e^+e^- \to J/\psi X^*(3860)(\to D\bar{D})$.

Source	Error
Nonresonant amplitude model	$^{+10.3}_{-0.0}\%$
Optimization	$^{+0.0}_{-5.1}\%$
Background mass calculation	$^{+2.1}_{-0.0}\%$
Training and testing difference	$<0.1\%$
Signal PDF statistical error	$^{+5.6}_{-5.8}\%$
Luminosity	$\pm1.4\%$
Tracking	$\pm1.7\%$
J/ψ and D branching fractions	$\pm3.3\%$
Particle identification	$\pm4.3\%$
K^0_S reconstruction	$\pm0.4\%$
π^0 reconstruction	$\pm0.4\%$
Total	$^{+13.2}_{-9.7}\%$

VII. CONCLUSIONS AND DISCUSSION

In summary, a new charmoniumlike state, the $X^*(3860)$, is observed in the process $e^+e^- \to J/\psi D\bar{D}$. The $X^*(3860)$ mass is (3862^{+26+40}_{-32-13}) MeV/c^2 and its width is $(201^{+154+88}_{-67-82})$ MeV. The $J^{PC} = 0^{++}$ hypothesis is favored over the 2^{++} hypothesis at the level of 2.5σ.

The new state $X^*(3860)$ seems to be a better candidate for the $\chi_{c0}(2P)$ charmonium state than the $X(3915)$, since its properties are well matched to expectations for the $\chi_{c0}(2P)$ resonance. The preferred quantum numbers of the $X^*(3860)$ are $J^{PC} = 0^{++}$, although the 2^{++} hypothesis is not excluded. The measured $X^*(3860)$ mass is close to potential model expectations for the $\chi_{c0}(2P)$. For example, the predicted mass in the Ebert-Faustov-Galkin model is 3854 MeV/c^2 [44]. Although the Godfrey-Isgur model [45] prediction (3916 MeV/c^2) is somewhat higher, the differences between this model's predicted and the observed masses for the established $\chi_{c2}(2P)$ and $\psi(4040)$ charmonium states are also high by a similar amount ($\sim$60 MeV/c^2). Potential models generally predict that the value of the mass-splitting ratio

$$r_c = \frac{m_{\chi_{c2}(2P)} - m_{\chi_{c0}(2P)}}{m_{\chi_{c2}(1P)} - m_{\chi_{c0}(1P)}} \qquad (28)$$

lies between 0.6 and 0.9 [11]; if the $X^*(3860)$ is indeed the $\chi_{c0}(2P)$, then $r_c = 0.46^{+0.25}_{-0.34}$. As a conventional charmonium state above the $D\bar{D}$ threshold, the $\chi_{c0}(2P)$ is expected to decay primarily to $D\bar{D}$, which coincides with our observed decay mode of the $X^*(3860)$ [unlike the $X(3915)$, where the $D\bar{D}$ mode has not been seen and the actual $J/\psi\omega$ observation mode is expected to be OZI-suppressed for the $\chi_{c0}(2P)$]. The $X^*(3860)$ helicity amplitudes are consistent with pure S-wave production. An angular analysis of the related process $e^+e^- \to J/\psi\chi_{c0}(1P)$ was performed in Ref. [43]; the angular distribution of this process was also found to be consistent with pure S-wave production. Note that while the production amplitudes for the $X^*(3860)$ and $\chi_{c0}(1P)$ are in mutual agreement, they do not agree with the NRQCD prediction [35]. In addition, the $X^*(3860)$ mass and width agree with the $\chi_{c0}(2P)$ parameters determined from an alternative fit to the Belle and *BABAR* $\gamma\gamma \to D\bar{D}$ data performed in Ref. [8]: $M = (3837.6 \pm 11.5)$ MeV/c^2, $\Gamma = (221 \pm 19)$ MeV.

ACKNOWLEDGEMENT

We thank the KEKB group for the excellent operation of the accelerator; the KEK cryogenics group for the efficient operation of the solenoid; and the KEK computer group, the National Institute of Informatics, and the PNNL/EMSL computing group for valuable computing and SINET5 network support. We acknowledge support from the Ministry of Education, Culture, Sports, Science, and Technology (MEXT) of Japan, the Japan Society for the Promotion of Science (JSPS), and the Tau-Lepton Physics Research Center of Nagoya University; the Australian Research Council; Austrian Science Fund under Grant No. P 26794-N20; the National Natural Science Foundation of China under Contracts No. 10575109, No. 10775142, No. 10875115, No. 11175187, No. 11475187, No. 11521505 and No. 11575017; the Chinese Academy of Science Center for Excellence in Particle Physics; the Ministry of Education, Youth and Sports of the Czech Republic under Contract No. LTT17020; the Carl Zeiss Foundation, the Deutsche Forschungsgemeinschaft, the Excellence Cluster Universe, and the VolkswagenStiftung; the Department of Science and Technology of India; the Istituto Nazionale di Fisica Nucleare of Italy; the WCU program of the Ministry of Education, National Research Foundation (NRF) of Korea Grants No. 2011-0029457, No. 2012-0008143, No. 2014R1A2A2A01005286, No. 2014R1A2A2A01002734, No. 2015R1A2A2A01003280, No. 2015H1A2A1033649, No. 2016R1D1A1B01010135, No. 2016K1A3A7A09005603, No. 2016K1A3A7A09005604, No. 2016R1D1A1B02012900, No. 2016K1A3A7A09005606, No. NRF-2013K1A3A7A06056592; Korean Institute for Basic Science Project Code IBS-R016-D1; the Brain Korea 21-Plus program, Radiation Science Research Institute, Foreign Large-size Research Facility Application Supporting project and the Global Science Experimental Data Hub Center of the Korea Institute of Science and Technology Information; the Polish Ministry of Science and Higher Education and the National Science Center; the Ministry of Education and Science of the Russian Federation under Contracts No. 14.A12.31.0006 and No. 3.2989.2017 and the Russian Foundation for Basic Research; the Slovenian Research Agency; Ikerbasque, Basque Foundation for Science and the Euskal Herriko Unibertsitatea (UPV/EHU) under program UFI 11/55 (Spain); the Swiss National Science Foundation; the Ministry of Education and the Ministry of Science and Technology of Taiwan; and the U.S. Department of Energy and the National Science Foundation.

Appendix A: Derivation of the signal density function

The signal density function is calculated for the process $e^+e^- \to J/\psi X^*$, with $J/\psi \to \ell^+\ell^-$ and $X^* \to D\bar{D}$. The definition of the production angle $\theta_{\rm prod}$ is shown in Fig. 8. This angle is given by

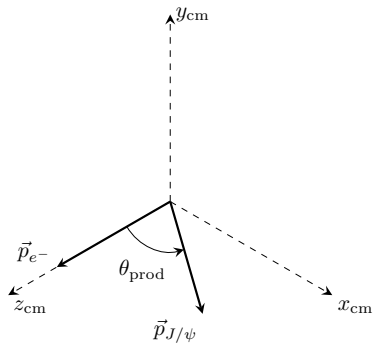

FIG. 8. Definition of the production angle (in the e^+e^- center-of-mass frame).

$$\cos\theta_{\rm prod} = \frac{\vec{p}_{e^-} \cdot \vec{p}_{J/\psi}}{|\vec{p}_{e^-}||\vec{p}_{J/\psi}|}, \tag{A1}$$

where $\vec{p}_{e^-}$ and $\vec{p}_{J/\psi}$ are the momenta of the beam e^- and J/ψ, respectively, in the center-of-mass frame.

The definitions of the J/ψ helicity angle and the ℓ^- azimuthal angle are shown in Fig. 9. The J/ψ helicity

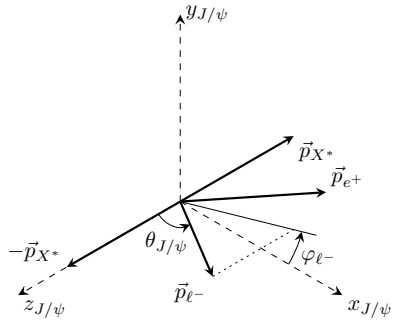

FIG. 9. Definitions of the J/ψ helicity angle and the angle φ_{ℓ^-} (in the J/ψ rest frame).

angle is given by

$$\cos\theta_{J/\psi} = -\frac{\vec{p}_{X^*} \cdot \vec{p}_{\ell^-}}{|\vec{p}_{X^*}||\vec{p}_{\ell^-}|}, \tag{A2}$$

where $\vec{p}_{X^*}$ and $\vec{p}_{\ell^-}$ are the momenta of X^* and ℓ^-, respectively, in the J/ψ rest frame. The azimuthal angle φ_{ℓ^-} can be expressed as

$$\begin{aligned}\cos\varphi_{\ell^-} &= \frac{\vec{a}_{e^+}\cdot\vec{a}_{\ell^-}}{|\vec{a}_{e^+}||\vec{a}_{\ell^-}|},\\ \sin\varphi_{\ell^-} &= -\frac{[\vec{p}_{X^*}\times\vec{a}_{e^+}]\cdot\vec{a}_{\ell^-}}{|\vec{p}_{X^*}||\vec{a}_{e^+}||\vec{a}_{\ell^-}|},\end{aligned} \tag{A3}$$

where

$$\begin{aligned}\vec{a}_{e^+} &= \vec{p}_{e^+} - \frac{\vec{p}_{e^+}\cdot\vec{p}_{X^*}}{|\vec{p}_{X^*}|^2}\vec{p}_{X^*},\\ \vec{a}_{\ell^-} &= \vec{p}_{\ell^-} - \frac{\vec{p}_{\ell^-}\cdot\vec{p}_{X^*}}{|\vec{p}_{X^*}|^2}\vec{p}_{X^*},\end{aligned} \tag{A4}$$

with $\vec{p}_{e^+}$ denoting the momentum of a beam positron in the J/ψ rest frame.

The coordinate system $(x_{\rm cm}, y_{\rm cm}, z_{\rm cm})$ is rotated by $\theta_{\rm prod}$ around the y axis and boosted to the J/ψ or X^* rest frame. For the J/ψ, the resulting coordinate system $(x_{J/\psi}, y_{J/\psi}, z_{J/\psi})$ has normal orientation: the J/ψ helicity quantization axis is the same as $z_{J/\psi}$. For the X^*, the resulting coordinate system $(x_{X^*}, y_{X^*}, z_{X^*})$ has inverse orientation: the helicity quantization axis is antiparallel to the z_{X^*} axis. The latter coordinate system is shown in Fig. 10. One can perform a rotation to

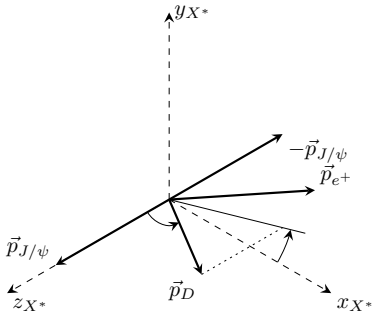

FIG. 10. The coordinate system $(x_{X^*}, y_{X^*}, z_{X^*})$ (in the X^* rest frame).

the D helicity frame directly from the coordinate system $(x_{X^*}, y_{X^*}, z_{X^*})$; however, this results in a nonstandard definition of the helicity and azimuthal angles as well as a sign flip for the X^* helicity in the amplitude. To conform to standard definitions, the coordinate system $(x_{X^*}, y_{X^*}, z_{X^*})$ is rotated by π around the z axis and by π around the y axis. The direction of the z'_{X^*} axis of the resulting coordinate system $(x'_{X^*}, y'_{X^*}, z'_{X^*})$ is opposite the direction of the z_{X^*}; the direction of the x axis is the same. The amplitude corresponding to this rotation is

$$\begin{aligned}A_{\lambda_{X^*}\,\tilde{\lambda}_{X^*}} &= D^{J(X^*)\,*}_{-\lambda_{X^*}\lambda_{X^*}}(\pi,\pi,0)\\ &= e^{-i\lambda_{X^*}\pi} d^{J(X^*)}_{-\lambda_{X^*}\,\lambda_{X^*}}(\pi) = (-1)^{J(X^*)},\end{aligned} \tag{A5}$$

where λ_{X^*} is the X^* helicity. Thus, the amplitude of the additional rotation merely introduces a common term for all X^* helicity amplitudes and can be omitted. Note that the amplitude of the process $B^+ \to X(\to J/\psi(\to \mu^+\mu^-)\phi(\to K^+K^-))K^+$ in Ref. [46] is defined in a similar way without the additional term $(-1)^{J(\phi)}$.

The definitions of the X^* helicity angle and the D azimuthal angle are shown in Fig. 11. The X^* helicity angle

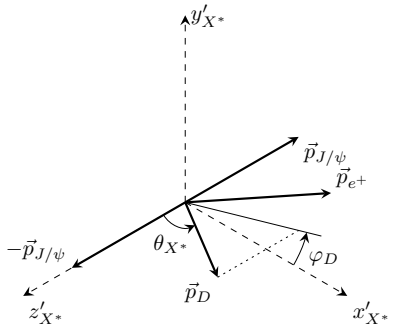

FIG. 11. Definitions of the X^* helicity angle and the angle φ_D (in the X^* rest frame).

is given by

$$\cos\theta_{X^*} = -\frac{\vec{p}_{J/\psi}\cdot\vec{p}_D}{|\vec{p}_{J/\psi}||\vec{p}_D|}, \tag{A6}$$

where $\vec{p}_{J/\psi}$ and $\vec{p}_D$ are the momenta of J/ψ and D, respectively, in the X^* rest frame. Note that $\vec{p}_D$ is the momentum of the reconstructed D meson; it changes to $\vec{p}_{\bar{D}}$ if the $\bar{D}$ meson is reconstructed. The azimuthal angle φ_D can be expressed as

$$\begin{aligned}\cos\varphi_D &= \frac{\vec{a}_{e^+}\cdot\vec{a}_D}{|\vec{a}_{e^+}||\vec{a}_D|},\\ \sin\varphi_D &= -\frac{[\vec{p}_{J/\psi}\times\vec{a}_{e^+}]\cdot\vec{a}_D}{|\vec{p}_{J/\psi}||\vec{a}_{e^+}||\vec{a}_D|}.\end{aligned} \tag{A7}$$

where

$$\begin{aligned}\vec{a}_{e^+} &= \vec{p}_{e^+} - \frac{\vec{p}_{e^+}\cdot\vec{p}_{J/\psi}}{|\vec{p}_{J/\psi}|^2}\vec{p}_{J/\psi},\\ \vec{a}_D &= \vec{p}_D - \frac{\vec{p}_D\cdot\vec{p}_{J/\psi}}{|\vec{p}_{J/\psi}|^2}\vec{p}_{J/\psi},\end{aligned} \tag{A8}$$

with $\vec{p}_{e^+}$ denoting the momentum of a beam positron in the J/ψ rest frame.

The amplitude is given by

$$\begin{aligned}&A_{\lambda_{\rm beam}\,\lambda_{J/\psi}\,\lambda_{X^*}\,\lambda_{\ell\ell}}(\Phi)\\ &\quad= H_{\lambda_{J/\psi}\,\lambda_{X^*}} d^1_{\lambda_{\rm beam}\,\lambda_{J/\psi}-\lambda_{X^*}}(\theta_{\rm prod}) e^{i\lambda_{J/\psi}\varphi_{\ell^-}}\\ &\qquad\times d^1_{\lambda_{J/\psi}\,\lambda_{\ell\ell}}(\theta_{J/\psi}) e^{i\lambda_{X^*}\varphi_D} d^{J(X^*)}_{\lambda_{X^*}\,0}(\theta_{X^*}),\end{aligned} \tag{A9}$$

and

$$A_{\lambda_{\rm beam}\,\lambda_{\ell\ell}}(\Phi) = \sum_{\substack{\lambda_{J/\psi}=-1,0,1\\ \lambda_{X^*}=-J(X^*),\ldots,J(X^*)}} A_{\lambda_{\rm beam}\,\lambda_{J/\psi}\,\lambda_{X^*}\,\lambda_{\ell\ell}}(\Phi) \quad \text{(A10)}$$

where $H_{\lambda_{J/\psi}\,\lambda_{X^*}}$ is the production helicity amplitude, λ is the helicity of the particle specified by the index, $\lambda_{\rm beam}$ is the sum of helicities of the beam electron and positron and $\lambda_{\ell\ell}$ is the sum of the helicities of the J/ψ decay products.

The X^* spin and parity are related:

$$P(X^*) = (-1)^{J(X^*)}. \quad \text{(A11)}$$

The helicity amplitudes are related due to parity conservation; taking into account Eq. (A11), the relation is

$$H_{-\lambda_{J/\psi}\,-\lambda_{X^*}} = H_{\lambda_{J/\psi}\,\lambda_{X^*}}, \quad \text{(A12)}$$

independent of $J(X^*)$. An additional selection rule is

$$|\lambda_{J/\psi} - \lambda_{X^*}| \leq 1. \quad \text{(A13)}$$

The lepton pair is produced in the electromagnetic decay $J/\psi \to \ell^+\ell^-$ via a virtual photon; thus, its helicity $\lambda_{\ell\ell}$ may be equal to 1 or -1. In the case of one-photon exchange (for positive C-parity of X), the beam helicity is also equal to 1 or -1.

The amplitude is additionally constrained due to C-parity conservation. The $D\bar{D}$ system has $C = (-1)^{J(X^*)}$; as its C-parity should be positive in case of one-photon production, odd values of $J(X^*)$ are forbidden. Thus, only two hypotheses, $J(X^*) = 0$ and $J(X^*) = 2$, are considered.

The signal density function is

$$S(\Phi) = \sum_{\substack{\lambda_{\rm beam}=-1,1\\ \lambda_{\ell\ell}=-1,1}} \left| \sum_{X^*} A_{\lambda_{\rm beam}\,\lambda_{\ell\ell}}(\Phi) A_{X^*}(M_{D\bar{D}}) \right|^2, \quad \text{(A14)}$$

where X^* is any contribution to the signal (X^* resonance or nonresonant amplitude). If the reconstructed particle is $\bar{D}$ instead of D, the angles θ_{X^*} and φ_D can be calculated from the angles for the reconstructed $\bar{D}$: $\theta_{X^*} \to \pi - \theta_{X^*}$, $\varphi_D \to \varphi_D + \pi$ (see Fig. 11). However, it is not necessary to perform this substitution, as the resulting signal density is exactly the same.

For $J(X^*) = 0$, there are two helicity amplitudes: $H_{0\,0}$ and $H_{1\,0}$. For $J(X^*) = 2$, there are five helicity amplitudes: $H_{0\,0}$, $H_{1\,0}$, $H_{0\,1}$, $H_{1\,1}$ and $H_{1\,2}$. The helicity amplitudes can be expressed in terms of partial wave amplitudes $L(J/\psi, X^*)_{J(J/\psi,X^*)}$ using Eq. (B5) from Ref. [47]. For $J(X^*) = 0$, the relations are (partial wave amplitudes forbidden by parity conservation being omitted):

$$\begin{aligned} H_{0\,0} &= \sqrt{\frac{1}{3}} S_1 - \sqrt{\frac{2}{3}} D_1, \\ H_{1\,0} &= \sqrt{\frac{1}{3}} S_1 + \sqrt{\frac{1}{6}} D_1. \end{aligned} \quad \text{(A15)}$$

[1] K. Abe *et al.* (Belle Collaboration), Phys. Rev. Lett. **94**, 182002 (2005).
[2] B. Aubert *et al.* (*BABAR* Collaboration), Phys. Rev. Lett. **101**, 082001 (2008).
[3] P. del Amo Sanchez *et al.* (*BABAR* Collaboration), Phys. Rev. D **82**, 011101 (2010).
[4] S. Uehara *et al.* (Belle Collaboration), Phys. Rev. Lett. **104**, 092001 (2010).
[5] J. P. Lees *et al.* (*BABAR* Collaboration), Phys. Rev. D **86**, 072002 (2012).
[6] K. A. Olive *et al.* (Particle Data Group), Chin. Phys. C **38**, 090001 (2014).
[7] S. Okubo, Phys. Lett. **5**, 165 (1963); G. Zweig, CERN Report Th 401 and 412 (1964); J. Iizuka, K. Okada and O. Shito, Prog. Theor. Phys. **35**, 1061 (1966); J. Iizuka, Prog. Theor. Phys. Suppl. **37**, 21 (1966).
[8] F. K. Guo and U. G. Meissner, Phys. Rev. D **86**, 091501 (2012).
[9] T. Barnes, S. Godfrey and E. S. Swanson, Phys. Rev. D **72**, 054026 (2005).
[10] E. J. Eichten, K. Lane and C. Quigg, Phys. Rev. D **69**, 094019 (2004).
[11] S. L. Olsen, Phys. Rev. D **91**, 057501 (2015).
[12] Z. Y. Zhou, Z. Xiao and H. Q. Zhou, Phys. Rev. Lett. **115**, 022001 (2015).
[13] C. Patrignani *et al.* (Particle Data Group), Chin. Phys. C **40**, 100001 (2016).
[14] S. Uehara *et al.* (Belle Collaboration), Phys. Rev. Lett. **96**, 082003 (2006).
[15] B. Aubert *et al.* (*BABAR* Collaboration), Phys. Rev. D **81**, 092003 (2010).
[16] G. T. Bodwin, J. Lee and E. Braaten, Phys. Rev. D **67**, 054023 (2003); Erratum: Phys. Rev. D **72**, 099904 (2005).
[17] G. T. Bodwin, J. Lee and E. Braaten, Phys. Rev. Lett. **90**, 162001 (2003).
[18] S. Uehara *et al.* (Belle Collaboration), PTEP **2013**, 123C01 (2013).
[19] K. Abe *et al.* (Belle Collaboration), Phys. Rev. Lett. **98**, 082001 (2007).
[20] P. Pakhlov *et al.* (Belle Collaboration), Phys. Rev. Lett. **100**, 202001 (2008).
[21] S. Kurokawa and E. Kikutani, Nucl. Instrum. Methods Phys. Res., Sect. A **499**, 1 (2003), and other papers included in this Volume; T. Abe *et al.*, Prog. Theor. Exp. Phys. **2013**, 03A001 (2013) and references therein.
[22] A. Abashian *et al.* (Belle Collaboration), Nucl. Instrum. Methods Phys. Res., Sect. A **479**, 117 (2002); also see detector section in J. Brodzicka *et al.*, Prog. Theor. Exp. Phys. **2012**, 04D001 (2012).
[23] Z. Natkaniec *et al.* (Belle SVD2 Group), Nucl. Instrum. Methods Phys. Res., Sect. A **560**, 1 (2006).
[24] R. Brun *et al.*, GEANT 3.21, CERN DD/EE/84-1, 1984.
[25] K. Hanagaki, H. Kakuno, H. Ikeda, T. Iijima and T. Tsukamoto, Nucl. Instrum. Methods Phys. Res., Sect. A **485**, 490 (2002).

[26] A. Abashian *et al.*, Nucl. Instrum. Methods Phys. Res., Sect. A **491**, 69 (2002).
[27] H. Voss, A. Hocker, J. Stelzer and F. Tegenfeldt, PoS ACAT, 040 (2007).
[28] F. Campanario, H. Czy, J. Gluza, M. Gunia, T. Riemann, G. Rodrigo and V. Yundin, JHEP **1402**, 114 (2014).
[29] D. J. Lange, Nucl. Instrum. Methods Phys. Res., Sect. A **462**, 152 (2001).
[30] T. Skwarnicki, Ph.D. Thesis, Institute for Nuclear Physics, Krakow 1986; DESY Internal Report, DESY F31-86-02 (1986).
[31] M. Williams, JINST **5**, P09004 (2010).
[32] G. Punzi, eConf C **030908**, MODT002 (2003).
[33] E. A. Kuraev and V. S. Fadin, Sov. J. Nucl. Phys. **41**, 466 (1985).
[34] J. Blatt and V. Weisskopf, *Theoretical Nuclear Physics* (John Wiley & Sons, New York, 1952), p. 361.
[35] K. Y. Liu, Z. G. He and K. T. Chao, Phys. Rev. D **77**, 014002 (2008).
[36] Victor Chernyak, private communication based on A. E. Bondar and V. L. Chernyak, Phys. Lett. B **612**, 215 (2005).
[37] Christoph Hanhart, private communication based on C. Hanhart, Phys. Lett. B **715**, 170 (2012).
[38] A. Garmash *et al.* (Belle Collaboration), Phys. Rev. D **71**, 092003 (2005).
[39] S. S. Wilks, Annals Math. Statist. **9**, 60 (1938).
[40] R. Aaij *et al.* (LHCb Collaboration), Phys. Rev. Lett. **112**, 222002 (2014).
[41] C. B. Lang, L. Leskovec, D. Mohler and S. Prelovsek, JHEP **1509**, 089 (2015).
[42] S. Ryu *et al.* (Belle Collaboration), Phys. Rev. D **89**, 072009 (2014).
[43] K. Abe *et al.* (Belle Collaboration), Phys. Rev. D **70**, 071102 (2004).
[44] D. Ebert, R. N. Faustov and V. O. Galkin, Phys. Rev. D **67**, 014027 (2003).
[45] S. Godfrey and N. Isgur, Phys. Rev. D **32**, 189 (1985).
[46] R. Aaij *et al.* (LHCb Collaboration), Phys. Rev. D **95**, 012002 (2017).
[47] M. Jacob and G. C. Wick, Annals Phys. **7**, 404 (1959) [Annals Phys. **281**, 774 (2000)].